



Fatigue of additively manufactured 316L stainless steel: The influence of porosity and surface roughness

Klas Solberg¹  | Shuai Guan² | Seyed Mohammad Javad Razavi¹  | Torgeir Welo¹ | Kang Cheung Chan² | Filippo Berto¹ 

¹ Department of Mechanical and Industrial Engineering, Norwegian University of Science and Technology, Trondheim, Norway

² Department of Industrial and Systems Engineering, The Hong Kong Polytechnic University, Hong Kong

Correspondence

Klas Solberg, Department of Mechanical and Industrial Engineering, Norwegian University of Science and Technology, Richard Birkelandsvei 2b, Trondheim 7034, Norway.

Email: klas.solberg@ntnu.no

Funding information

Hong Kong Polytechnic University; Norges Teknisk-Naturvitenskapelige Universitet

Abstract

The fatigue behaviour of additively manufactured (AM) 316L stainless steel is investigated with the main emphasis on internal porosity and surface roughness. A transition between two cases of failure are found: failure from defects in the surface region and failure from the internal defects. At low applied load level (and consequently a high number of cycles to failure), fatigue is initiating from defects in the surface region, while for high load levels, fatigue is initiating from internal defects. Porosities captured by X-ray computed tomography (XCT) are compared with the defects initiating fatigue cracks, obtained from fractography. The fatigue data are synthesised using stress intensity factor (SIF) of the internal and surface defects on the fracture surface.

KEYWORDS

316L stainless steel, fatigue, porosity, selective laser melting, surface roughness

1 | INTRODUCTION

Additive manufacturing (AM) is a processing method capable of producing parts by adding material layer-by-layer, controlled by computer-assisted codes.^{1–3} AM allows for producing components with high geometric complexity, including internal structures and undercuts in one step without postprocessing.^{4,5} In recent years, AM is becoming accepted as a manufacturing method

for industries like aerospace, medical, energy, and automotive.^{6,7} However, there are some challenges when dealing with AM. Properties deriving from the processing method such as voids, high surface roughness, residual stresses, and anisotropic microstructure can affect the overall mechanical behaviour of these components.^{1,2} Especially when dealing with fatigue, the geometrical discontinuities, such as porosities or defects in the surface region, are factors strongly affecting the performance.^{6,8,9}

316L is an austenitic chromium-nickel stainless steel. It is one of the most widely used stainless steels due to its good ductility, high strength, and high corrosion resistance.^{6,7} It is used in engineering applications such as automobile, oil and gas, construction, chemical, and petrochemical industries.^{6,7} Dealing with AM 316L, it has shown higher strength than its conventionally manufactured counterparts, where a lower ductility has

Nomenclature: A_d , defect area; A_{eff} , effective defect area; c , surface defect depth; E , energy density; h , failure site along build orientation; h_0 , length of gauge section; K_{max} , Mmaximum stress intensity factor; k , inverse slope; l , hatch distance; N_f , number of cycles to failure; P , laser power; R , loading ratio; t , layer thickness; T_σ , T_K , scatter index; v , scanning speed; ΔK , stress intensity factor range; ΔK_{th} , threshold of stress intensity factor range; σ_{max} , maximum stress; σ_{min} , minimum stress; σ_{nom} , nominal stress; σ_{UTS} , ultimate tensile strength.

This is an open access article under the terms of the Creative Commons Attribution License, which permits use, distribution and reproduction in any medium, provided the original work is properly cited.

©2019 The Authors Fatigue & Fracture of Engineering Materials & Structures Published by John Wiley & Sons Ltd.

been reported.⁷ The higher strength in the as-built condition is attributed to a refined microstructure and a high dislocation density.⁷ In the as-built condition, the material display anisotropic mechanical properties, hot isostatic pressing (HIP) and heat treatments can remove anisotropy; it is also leading to a reduction of strength and increased ductility compared with as-built.¹⁰ The fatigue behaviour of as-built AM 316L steel has previously been investigated.^{11–14} The as-built specimens display lower fatigue life than their conventionally manufactured counterparts due to defects deriving from the manufacturing process.^{14–16} Further, postprocessed specimens have been shown to exceed the fatigue life of their conventionally manufactured counterparts.¹⁴

In the present work, 316L stainless steel produced by selective laser melting (SLM), a powder bed fusion (PBF) method, is investigated. The main objective of this work is to evaluate the effect of internal porosity and surface roughness on the fatigue behaviour, with the main emphasis on the interaction between these two. A series of 316L specimens produced by SLM is tested under static and uniaxial fatigue loading. The specimens were analysed employing X-ray computed tomography (XCT), displaying high amounts of porosities. The fracture surfaces were captured in scanning electron microscopy (SEM), and the results were not according to the typical results on AM metals. A transition between failure from surface defects and internal defects was observed. For high stress levels and a low number of cycles, fatigue is initiating from regions of internal defects (voids) while for low stress levels and a high number of cycles to failure, fatigue is initiating from defects in the surface region. Further, the $\sqrt{\text{area}}$ -method,¹⁷ a popular method when dealing with fatigue assessment of AM metals,^{15,18–22} was employed in order to express the fatigue life curve in terms of stress intensity factor (SIF).

2 | MATERIALS AND EXPERIMENTAL PROCEDURE

Round hourglass-shaped specimens with a constant gauge section of 4.5-mm diameter according to ASTM E466-15²³ of 316L stainless steel were produced by SLM. The geometry and dimensions of the specimens are shown in Figure 1A. The process parameters used for manufacturing the specimens are specified in Table 1. The specimens were printed standing in the z -direction so that the layers were perpendicular to the loading direction. The specimens were manufactured with three contours and internal hatching. The scanning strategy is shown in Figure 1B.

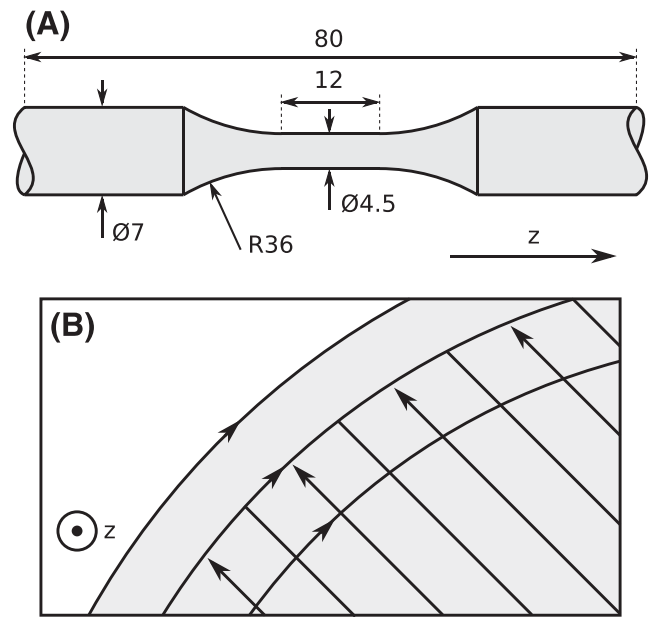


FIGURE 1 A, Geometry and dimensions of specimen, built layer-by-layer in z -direction. B, Schematic illustration of scanning strategy

TABLE 1 Process parameters used for fabrication of the specimens, layer thickness (t), hatch distance (l), scanning speed (v), laser power, (P) and energy density (E)

t [μm]	l [μm]	v [mm/s]	P [W]	E [W/mm ³]
50	100	2400	320	26.7

The surface roughness, R_a , was measured in the gauge section along the z -direction. An Alicona Infinity confocal microscope was used for the measurements. The reported value of R_a was taken as the average value of 12 measurements.

X-ray computed microtomography was conducted on a dual-tube micro-focus X-ray CT System YXLON FF35 CT. A cylindrical control volume with a diameter of 2 mm and a height of 1.65 mm was captured from the gauge section of a specimen. By employing an X-ray tube voltage of 195.0 kV, a current of 100.0 μA , a magnification of 52, and 1800 projections, a resolution of 2.7 μm was obtained. The same method as the one of Lu and Chan²⁴ was used.

A static tensile test with a loading rate of 0.3 mm/min was conducted to obtain the ultimate tensile strength, σ_{UTS} . Fatigue loading was done under load control with a loading ratio $R = \sigma_{min}/\sigma_{max} = 0.1$ and a frequency of 10 Hz. Fatigue data were presented in an S-N diagram, referring to the maximum nominal stress, σ_{max} . Haibach uniform confidence bands²⁵ at 10%, 50%, and 90% probability of failure was calculated according²⁶ to ISO 12107, ASTM E 739-

91,²⁷ from 10^4 to 2×10^6 cycles. From the confidence bands, the inverse slope, k , and the scatter index, $T_\sigma = \sigma_{90\%}/\sigma_{10\%}$, was obtained. The fatigue tests were discontinued when specimens had withstood 2×10^6 cycles without failure. Both static and fatigue tests were conducted on a servohydraulic MTS system with a load cell of 50 kN.

The fracture surfaces of all specimens were investigated by SEM. The defects initiating the fatigue cracks were captured and measured. This was done by identifying which regions showed signs of lack of fusion and unfused particles and which displayed crack growth. Based on this, a general outline of the defect region was obtained, and internal islands were excluded from the measurement. The effective area of the defects was also measured. The measurement was done according to the method of Murakami,¹⁷ which is further explained in Section 3.5. The failure initiation site along the build direction (z -axis in Figure 1A) was measured for all specimens.

3 | RESULTS

3.1 | Mechanical properties

The load-displacement curve from static loading is shown in Figure 2. From the static test, an ultimate tensile strength of 437 MPa was obtained. The results from the fatigue loading are shown in Figure 3. A fatigue strength of 163 MPa at 2×10^6 cycles was obtained, referring to the maximum stress, σ_{max} , applied.

3.2 | Fractography

For all the broken specimens, the fracture surfaces were examined. The specimens either showed fatigue initiation from internal defects or surface defects; one example of

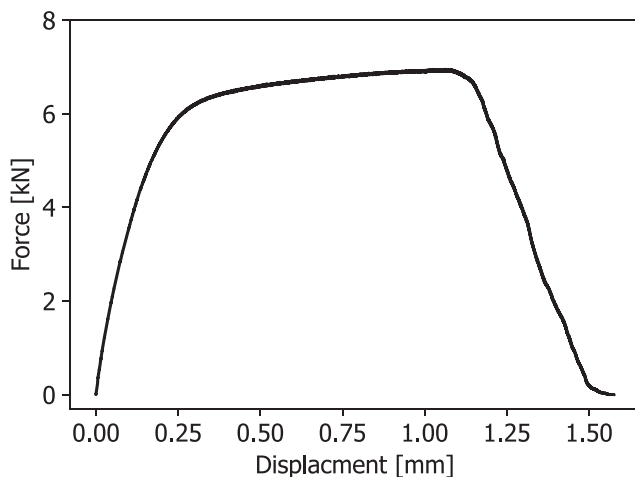


FIGURE 2 Load-displacement curve from static loading under displacement control

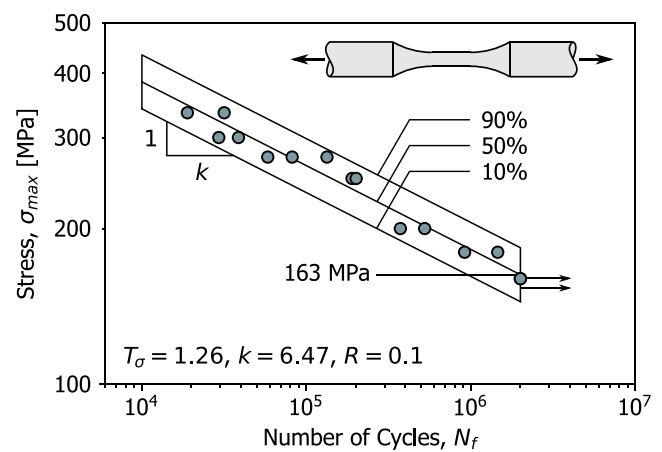


FIGURE 3 Fatigue data obtained from 316L stainless steel specimens, loading ratio $R=0.1$ [Colour figure can be viewed at wileyonlinelibrary.com]

each case is shown in Figure 4. Figure 4A to C shows failure from internal defects while Figure 4D to E shows failure from the surface defects.

In Figure 4A, the whole fracture surface of a specimen failing from internal defects is shown. A detail of the defect initiating fatigue is shown in Figure 4B, where both the unfused region with powder particles and the crack growth part (indicated by arrows) are visible. The transition from fatigue crack growth (striations) to final rupture (ductile) is shown in Figure 4C. In Figure 4D, the whole fracture surface of a specimen failing the surface is shown; the defect is shown with higher magnification in Figure 4E, where the arrows are indicating the crack growth. Sub-surface defects are present at $\sim 100 \mu\text{m}$ below the surface. Figure 4F shows a detail of the final rupture region, where the crack is occurring in steps over different layers. Unfused particles are shown in the different “layers” indicating the final rupture part is dominated by the interaction of defects.

A selection of six specimens ranging from static failure to High Cycle fatigue (HCF) is shown in Figure 5. The defects in the fracture surface are shaded and outlined by a white line. In the case of the fatigue loaded specimens, the crack growth is indicated by arrows, and a new line indicates the transition from crack growth to final rupture. Failure from static loading is shown in Figure 5A, the fracture surface displays a cup-cone morphology, and the core of the specimen displays several regions of defects. Several regions of defects are also seen in Figure 5B, where the specimen is failing in the low cycle fatigue regime. Two specimens failing from internal defects are shown in Figure 5C,D (Figure 5C being the same as Figure 4A). In Figure 5E,F, two specimens with fatigue initiating from the surface are shown (Figure 5E being the same as Figure 4E).

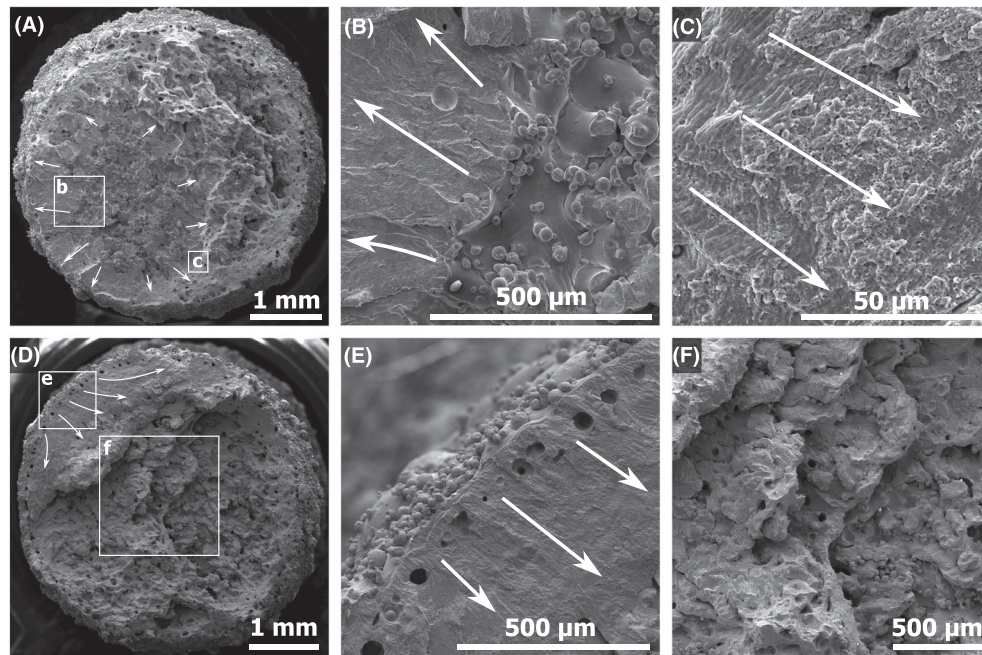


FIGURE 4 Scanning electron microscopy (SEM) of the two specimens: A, whole fracture surface of specimen failing from internal defect; B, detail from initiation; C, transition from striations to ductile failure; D, whole fracture surface of specimen failing from surface defect; E, detail of defect at fatigue initiation; F, detail from final rupture. The arrows are indicating the direction of crack propagation

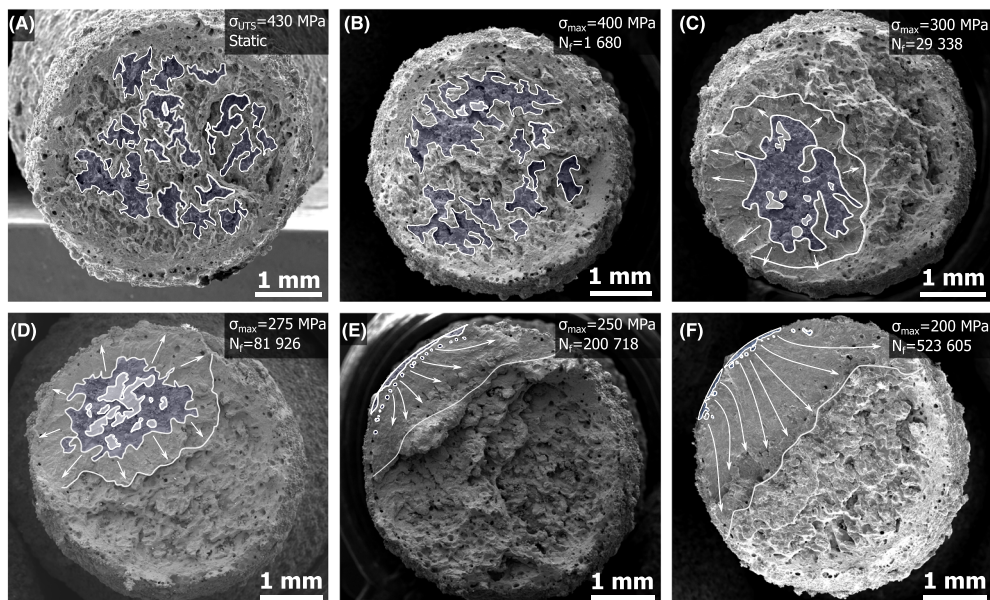


FIGURE 5 Fracture surfaces at different load levels: A, static; B, below HCF; C and D, internal defects and upper part of HCF; E and F, surface defects and lower part of HCF [Colour figure can be viewed at wileyonlinelibrary.com]

The area of defects found in the fracture surfaces was measured and correlated to the fatigue behaviour; this is shown in Figure 6A,B. A transition between failure from surface defects and internal defects is shown, and the shade of the markers indicates the defect size obtained from the fracture surfaces.

An optical micrograph of a polished cross-section of a specimen that failed from fatigue is shown in

Figure 7. The corresponding fracture surface is shown in Figure 5F. The crack is propagating from the left side, towards the right. The final rupture part is in different levels and displays large deformation. Like for the fracture surfaces shown in Figure 5, sub-surface defects are present, followed by a section with a low amount of defects, and then a porous core as can be seen in Figure 7.

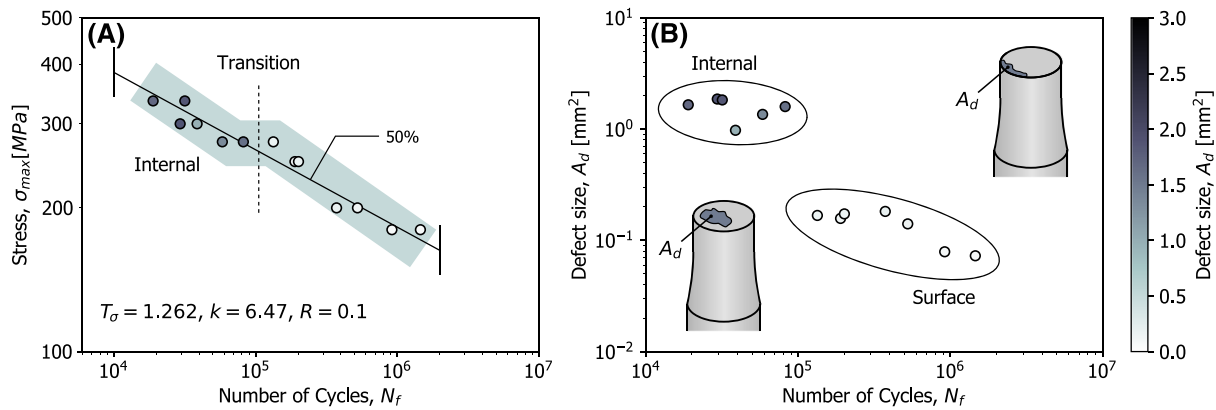


FIGURE 6 Fatigue behaviour correlated with defect size: A, S-N diagram with marker shade indicating defect size; B, defect size versus number of cycles to failure [Colour figure can be viewed at wileyonlinelibrary.com]

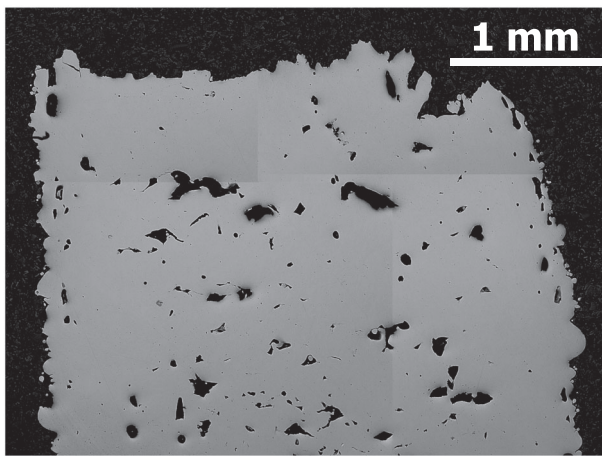


FIGURE 7 Polished cross section of a specimen subjected to fatigue. The corresponding fracture surface is shown in Figure 5F

3.3 | Failure initiation site

Recently, a diagram predicting the failure initiation location in AM metals was proposed.²⁸ The diagram is correlating the failure location, h/h_0 (in Figure 8), to the notch

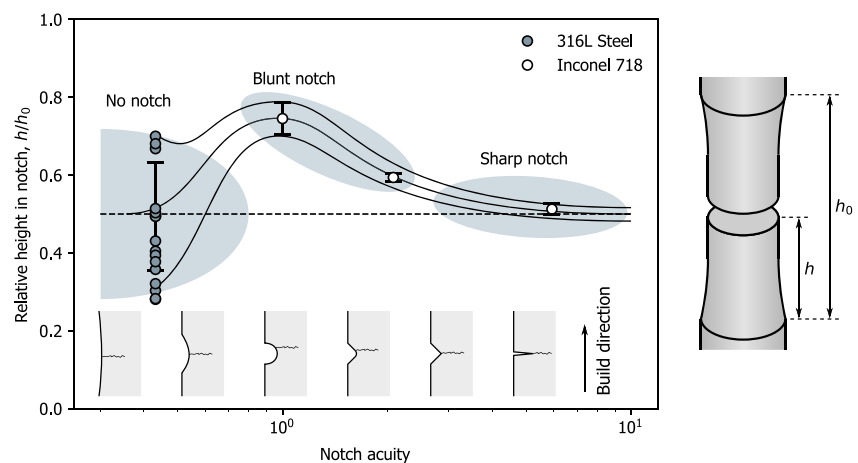
acuity and the surface roughness. Various notch geometries of as-built SLM Inconel 718 specimens were investigated, and the failure location was found to be dependent on the notch acuity and the amount of surface roughness adjacent to the notch root. Due to higher surface roughness in surfaces built downward-facing, failure did not occur at the notch root for blunt notches but from the region facing downward adjacent to the notch root. In addition, a large scatter in the failure location site was obtained for plain specimens, where the location of failure was found to be dependent on the location of the critical defects.

The failure location of the specimens investigated here was captured and compared with the plain specimen in the proposed diagram. This is shown in Figure 8. The specimens investigated here show a similar scatter as the Inconel specimens.

3.4 | Porosity and surface roughness

From the control volume examined by XCT-scan, a porosity of 5.4% was obtained. The results from the

FIGURE 8 Failure initiation site in additive manufacturing (AM) specimens versus notch acuity. Data from 316L stainless steel combined with AM Inconel 718 fatigue data from literature²⁸ [Colour figure can be viewed at wileyonlinelibrary.com]



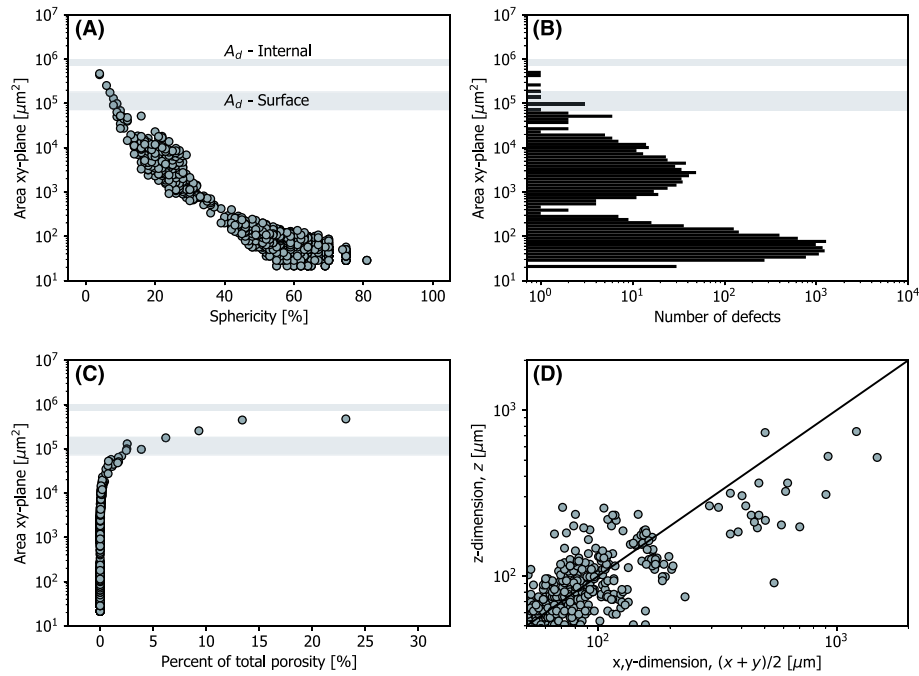


FIGURE 9 Porosity data from X-ray computed tomography (XCT) scan: A, area xy-plane versus sphericity; B, distribution of defects; C, size of defects as percent of total porosity volume; D, comparison of the defects x, y, and z-dimension. (The range of defect size measured from fracture surface in Figure 5 is indicated by shade in A-C) [Colour figure can be viewed at wileyonlinelibrary.com]

XCT scan are shown in Figure 9 compared with the defects found in the fracture surfaces (A_d). Figure 9A shows the projected area of the defects versus the sphericity of the defects. The main trend is that large defects have a low degree of sphericity, while small defects have a high degree of sphericity. Figure 9B shows the distribution of the defects, displaying two main bulks of defect sizes. Figure 9C shows the projected area versus the contribution of each defect to the total volume of defects. The most significant defect in the control volume makes a contribution of 23.2% to the total volume of defects.

From Figure 9A, the smaller defects are shown to have higher sphericity. Figure 9D shows a comparison of the x, y, and z-dimensions of the defects. The z-coordinate is compared with the average of x and y-coordinate in the upper range of defect sizes. For the larger defects, the average of x and y-dimension of the defect is larger than the z-dimension. This means that the smallest dimension of the defects is parallel to the loading direction; the same was observed in Figure 7 and in recent works dealing with defects in AM metals.^{15,20,29}

A surface roughness Ra of 10.1 was obtained from measurements using a confocal microscope.

3.5 | Application of SIF

The fatigue life curve was expressed in terms of SIF versus the number of cycles to failure. SIF can be applied

to a member containing defects by assuming that the crack size is equal to $\sqrt{\text{area}}$ of the defect obtained from the fracture surface so that SIFs can be approximated by¹⁷

$$K = Y\sigma\sqrt{\pi\sqrt{\text{area}}}. \quad (1)$$

Based on this formulation, two calculations were performed, considering the actual area of the defect size measured and considering the effective area (as in the original formulation by Murakami¹⁷). The geometry factor, Y , is 0.65 for surface defects and 0.5 for internal defects. Using the measured area, Equation (1) becomes

$$K_{\max} = Y\sigma_{\max}\sqrt{\pi\sqrt{A_d}}. \quad (2)$$

The result of the first calculation is shown in Figure 10 A. The transition between the surface defects and internal defects seen in the S-N curve is no longer present.

For the second calculation, the surface defects and the internal defects are considered based on two different formulations. For internal defects, an effective area, A_{eff} , is drawn around the defect area, while for surface defects, the depth of the defects, c , is captured, as shown in Figure 10D. Then, Equation (1) becomes

$$K_{\max} = Y\sigma_{\max}\sqrt{\pi\sqrt{A_{\text{eff}}}} \quad (\text{Internal defect}) \quad (3)$$

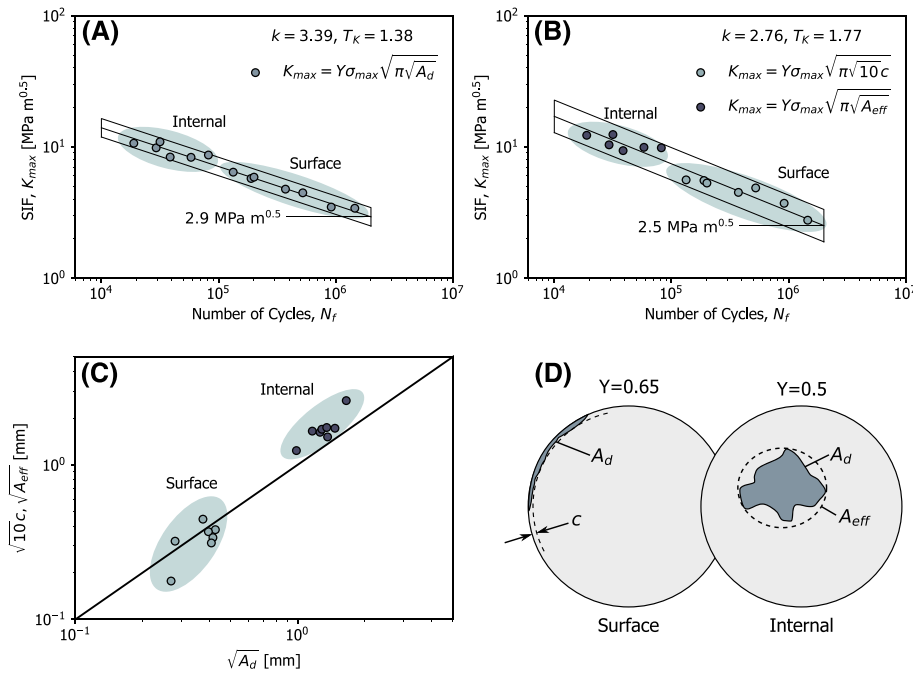


FIGURE 10 Application of stress intensity factor for initial defect in fracture surface: A, considering the actual measured area of defect; B, considering 10C and effective area; C, comparison between defect size in A and B; D, schematic illustration of defect and measured size [Colour figure can be viewed at wileyonlinelibrary.com]

and

$$K_{max} = Y \sigma_{max} \sqrt{\pi \sqrt{10c}} \quad (\text{Surface defect}). \quad (4)$$

The results are shown in Figure 10B. When comparing the results from the two calculations, the first method is showing a lower scatter. The size considered as crack length for the two cases is compared in Figure 10C.

4 | DISCUSSION

4.1 | Fatigue data and fractography

The fatigue behaviour of 316L specimens prepared by SLM has been investigated. Although the specimens contained high amounts of defects, the fatigue behaviour was found to be comparable with recently reported fatigue data on AM 316L. By employing the Smith-Watson-Topper (SWT) means stress correction,³⁰ the fatigue data reported here give a fatigue strength of 120 MPa under fully reversed loading ($R=-1$). The same mean stress correction is employed on fatigue data from the literature, giving a range of 100 to 300 MPa for AM as-built 316L steels^{13,14,31} and 300 to 420 MPa for wrought 316L steels.¹¹⁻¹³ The low fatigue strength obtained here is attributed to the high amount of defects and the high surface roughness in the specimens.

From the investigated specimens, two main categories of fatigue failure were observed: failure initiating from internal defects and failure initiating from surface defects. A transition between these two cases was observed in the number of cycles to failure. This trend indicates that for high loads, the internal defects were critical, while for low loads, the defects in the surface region were critical. For the specimens failing from above 10^5 cycles, fatigue initiates from the surface region. Similar results have been observed by Andreau et al¹⁵ stating that at approximately 10^6 cycles, surface defects are initiating fatigue, despite a presence of large internal defects.

The defects measured in the fracture surfaces were comparable with those obtained from XCT as seen in Figure 9A to C. The largest defects from XCT were in size-range between the surface and internal defects found in the fracture surface. When dealing with the defects from the fracture surface, there is a possibility that the measured defects are larger than the single defects obtained from XCT because there is a possibility of coalescence of defects adjacent to each other. This is illustrated schematically in Figure 11, where Figure 11A illustrates fatigue initiating from internal defects while Figure 11B illustrates fatigue initiating from the surface.

It is widely recognised that cracks and defects are decisive when dealing with fatigue. Fatigue usually initiate from defects, acting as local stress risers, if

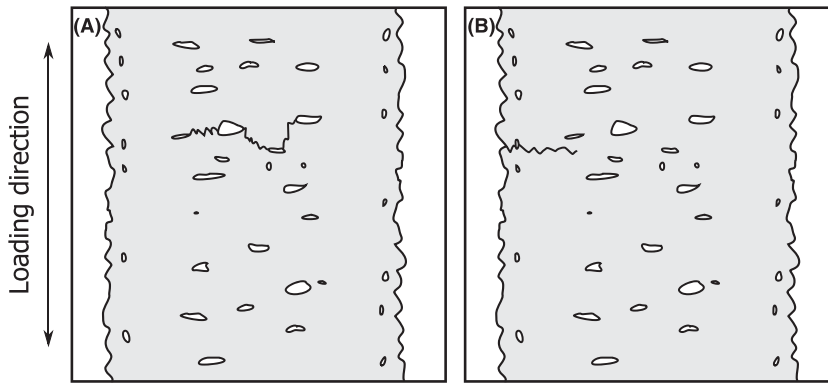


FIGURE 11 Failure mechanisms in specimens. Schematic illustration of A, failure from internal defects and B, failure from surface defects

present. Contrary in the case of static failure (especially for ductile materials), failure is not as closely linked to the localised defects as in fatigue. For static failure in ductile materials, failure is usually occurring by coalescence of voids involving plasticity.³² A transition between the interaction of defects to defects acting alone is expected when moving from static failure to high cycle fatigue. It is possible that the transition observed in the S-N curve is related to whether the defects are interacting or not.

Interaction between the defects can be observed in the final rupture part of the specimen shown in Figures 7 and 5F, where the fracture is occurring in different height steps. The fatigue crack initiates from the surface and propagates perpendicular to the z-direction, without jumping between layers, indicating that less interaction between the defects is involved.

4.2 | $\sqrt{\text{area}}$ -method

By employing the $\sqrt{\text{area}}$ -method, the fatigue life curve was expressed in terms of SIF. This was done both by considering the measured defect area and by considering the effective defect area and the surface defect depth. Comparing the results from the two cases, a lower scatter was obtained in the first method. Further, the step observed in the S-N diagram was removed when considering the measured defect area.

Fatigue crack growth of AM 316L steel in the as-built condition was studied by Riemer et al obtaining a SIF threshold, ΔK_{th} , of 4 MPa $\sqrt{\text{m}}$ for loading perpendicular to the build direction and 3 MPa $\sqrt{\text{m}}$ parallel to the build direction.³¹ In order to compare the results obtained here with the results of Riemer et al, the maximum SIF was converted to SIF range by $\Delta K = 0.9 K_{max}$. From this, ΔK is 2.6 and 2.3 at 2×10^6 for the two cases of SIF calculations considered here. This is lower but still comparable with the value of ΔK_{th} reported by Riemer et al. The lower value of SIF range reported

here can be due to several reasons. The $\sqrt{\text{area}}$ -method is an approximate method giving some indication of the equivalent SIF value, so some scatter and error should be expected. The size of the defects is large compared with the cross-sectional area (at least for the internal defects). Further, the microstructure has been reported to affect the SIF threshold for AM 316L steel.³¹

One advantage of using the effective area is that it can be more efficient than using the real area when measuring the defects manually based on fracture surfaces. A smoothly shaped geometry is drawn around the defect; this is done by various methods. One challenge by this method is that the defect size is not unambiguously defined. By using the real projected area of the defects, it is easier to define the defect size unambiguously. However, it is more time-consuming to define it manually. In the case of obtaining the defect size from XCT data, it is opposite from manual measurements; the real defect size can be extracted directly, while the effective area needs to be calculated.

By employing the $\sqrt{\text{area}}$ -method, the theory of linear elastic fracture mechanics is assumed to be valid. Under fatigue loading in the high cycle fatigue regime, cracks are propagating in a brittle manner, and a low amount of plasticity is involved. When the defects are not interacting and the failure is initiating from localised defects (and not a large region), SIF should be possible to apply. While when the defects are large compared with the cross section and there is a chance of several defects interacting, it is more uncertain whether it should be applied or not.

4.3 | Failure initiation site

The diagram in Figure 8 shows the failure initiation site in the 316L specimens investigated here compared with AM Inconel 718 specimens. The Inconel specimens were of different notch radii, notch depths, and notch opening angles, resulting in different notch acuity and different

amount of overhang in the region adjacent to the notch root. The 316L specimens are unnotched and have a constant cross-section in the gauge section, so a scatter in failure location is expected.

The diagram states that if a component contains a sharp notch, fatigue will most likely initiate from the notch root. While if the component contains no notch, the failure location is determined by the location of the critical defect. Because of this, a large scatter in failure location can be expected in plain specimens but on average failure initiates from the region with the lowest cross-sectional area (unless there is a problem with a specific layer in the build). For the cases in between these two extremes, failure initiates as a combination of the stress from the notch root and the localised defects from the manufacturing process.

Applying the diagram can give some idea of the quality and the features of a build. Based on the geometrical features of the components and the location of the failure, some idea about the distributions and location of critical defects can be obtained. Also, the interaction between notches and local defects deriving from the manufacturing process can be understood. This is especially interesting when dealing with builds containing downward facing surfaces.

5 | CONCLUSIONS

From the present work, the following conclusions can be drawn:


- The fatigue behaviour of 316L stainless steel specimens produced by SLM has been investigated with the main emphasis on the effect of surface roughness and porosity
- Fractography revealed that for the low load levels in the HCF regime, specimens failed from defects in the surface region, while the higher load levels, the specimens failed from internal defects. A transition between these two cases is visible in the fatigue life curve. This result indicates that the porosity and internal defects are controlling fatigue initiation at load levels above 275 MPa, while defects in the surface regime are controlling fatigue initiation at load levels below 275 MPa.
- XCT displayed unfavourable orientation of large defects, and the size of the defects was comparable with the defects found to initiate fatigue from fractography.
- The fatigue life curve has been expressed in terms of SIF based on $\sqrt{\text{area}}$ -method, by both considering the measured defect area and the effective defect area.

ACKNOWLEDGEMENTS

This project was funded by the Norwegian University of Science and Technology and The Hong Kong Polytechnic University. The authors would like to acknowledge Prof L.C. Chan and Dr X.Z. Lu for assistance with XCT scan.

ORCID

Klas Solberg  <https://orcid.org/0000-0002-1700-6420>

Seyed Mohammad Javad Razavi  <https://orcid.org/0000-0002-2574-065X>

Filippo Berto  <https://orcid.org/0000-0001-9676-9970>

REFERENCES

1. Debroy T, Wei HL, Zuback JS. Additive manufacturing of metallic components process, structure and properties. *Prog Mat Sci*. 2018;92:112-224.
2. Herzog D, Seyda V, Wycisk E, Emmelmann C. Additive manufacturing of metals. *Acta Mater*. 2016;117:371-392.
3. Frazier WE. Metal additive manufacturing. *A review Acta Mater*. 2016;117:371-392.
4. Langelaar M. Topology optimization of 3d self-supporting structures for additive manufacturing. *Addit Manuf*. 2016;12:60-70.
5. Atzeni E, Salmi A. Economics of additive manufacturing for end-usable metal parts. *Int J Adv Manuf Tech*. 2012;62(9):1147-1155.
6. Afkhami A, Dabiri M, Alavi SH, Bjork T, Salminen A. Fatigue characteristics of steels manufactured by selective laser melting. *Int J Fatigue*. 2019;122:72-83.
7. Shamsujjoha M, Agnew SR, Fitz-Gerald JM, Moore WR, Newman TA. High strength and 320 ductility of additively manufactured 316 l stainless steel explained. *Metall Mater Trans A*. 2018;49(7):3011-3027.
8. Lewandowski JJ, Sei M. Metal additive manufacturing: a review of mechanical 326 properties. *Annu Rev Mater Res*. 2016;46(1):151-186.
9. Li P, Warner D, Fatemi A, Phan N. Critical assessment of the fatigue performance of additively manufactured Ti6Al4 V and perspective for future research. *Int J Fatigue*. 2016;85:130-143.
10. Zhang M, Sun C-N, Zhang X, Wei J, Hardacre D, Li H. High cycle fatigue and ratcheting interaction of laser powder bed fusion stainless steel 316L: fracture behaviour and stress-based modelling. *Int J fatigue*. 2019;121:252-264.
11. Huang H, Wang Z, Lu J, Lu K. Fatigue behaviors of AISI 316L stainless steel with a gradient nanostructured surface layer. *Acta Mater*. 2015;87:150-160.
12. Roland T, Retraint D, Lu K, Lu J. Fatigue life improvement through surface nanostructuring of stainless steel by means of surface mechanical attrition treatment. *Script Mater*. 2006;54(11):1949-1954.
13. Mower TM, Long MJ. Mechanical behavior of additive manufactured, powder-bed laser-fused materials. *Mater Sci Eng A*. 2016;651:198-213.

14. Elangeswaran C, Cutolo A, Muralidharan GK, Formanoir C, Berto F, Vanmeensel K, Hooreweder BV. Effect of post-treatments on the fatigue behaviour of 316L stainless steel manufactured by laser powder bed fusion. *Int J Fatigue*. 2019;123:31-39.
15. Andreau O, Pessard E, Koutiri I, Penot J-D, Dupuy C, Saintier N, Peyre P. A competition between the contour and hatching zones on the high cycle fatigue behaviour of a 316L stainless steel: analyzed using x-ray computed tomography. *Mater Sci Eng A*. 2019;757:146-159.
16. Solberg K, Bero F. What is going on with fatigue of additively manufactured metals? *Mater Des Proc Comm*. 2019;1(2):e84.
17. Murakami Y. Chapter 2 - stress concentration. *Metal Fatigue*. Oxford: Elsevier Science Ltd; 2002:11-24.
18. Günther J, Krewerth D, Lippmann T, Leuders S, Tröster T. Fatigue life of additively manufactured Ti6Al4 V in the very high cycle fatigue regime. *Int J Fatigue*. 2017;94:236-245.
19. Tamas-Williams S, Withers P, Todd I, Prangnell P. The influence of porosity on fatigue crack initiation in additively manufactured titanium components. *Sci Rep*. 2017;7:7308.
20. Romano S, Brückner-Foit A, Brandão J, Gumpinger J, Ghidini T, Beretta S. Fatigue properties of AlSi10Mg obtained by additive manufacturing: defect-based modelling and prediction of fatigue strength. *Eng Fract Mech*. 2018;187:165-189.
21. Yamashita Y, Murakami T, Mihara R, Okada M, Murakami Y. Defect analysis and fatigue design basis for Ni-based superalloy 718 manufactured by selective laser melting. *Int J Fatigue*. 2018;117:485-495.
22. Meneghetti G, Rigon D, Gennari C. An analysis of defects influence on axial fatigue strength of maraging steel specimens produced by additive manufacturing. *Int J Fatigue*. 2019;118:54-64.
23. group ASTM. Standard practice for conducting force controlled constant amplitude axial fatigue tests of metallic materials. Standard ASTM E466-15, ASTM International; 2015.
24. Lu X, Chan L. Micromechanics-based damage model for failure prediction in cold forming. *Mater Sci Eng A*. 2017;690:120-131.
25. Haibach CME. The concept of uniform scatter bands for analyzing S-N curves of unnotched and notched specimens in structural steel. *ASTM STP 770*. 1982;770:549-571.
26. ISO. Metallic materials - fatigue testing - statistical planning and analysis of data. Standard ISO 12107; 2012.
27. ASTM E73910. Standard Practice for Statistical Analysis of Linear or Linearized Stress-Life (S-N) and Strain-Life (ϵ -N) Fatigue Data. Standard ASTM E739 - 10 ASTM International; 2015.
28. Solberg K, Berto F. Notch-defect interaction in additively manufactured Inconel 718. *Int J Fatigue*. 2019;122:35-45.
29. Romano S, Brando A, Gumpinger J, Gschweidl M, Beretta S.. Qualification of AM parts: extreme value statistics applied to tomographic measurements. *Mater Des*. 2017;131:32-48.
30. Smith K, Topper T, Watson P. A stress-strain function for the fatigue of metals (stress-strain function for metal fatigue including mean stress effect). *J Mater*. 1970;5:767-778.
31. Riemer A, Leuders S, Thöne M, Richard HA, Tröster T. On the fatigue crack growth behavior in 316L stainless steel manufactured by selective laser melting. *Eng Fract Mech*. 2014;120:15-25.
32. Tvergaard V, Needleman A. Analysis of the cup-cone fracture in a round tensile bar. *Act Metall*. 1984;32(1):157-169.

How to cite this article: Solberg K, Guan S, Razavi SMJ, Welo T, Chan KC, Berto F. Fatigue of additively manufactured 316L stainless steel: The influence of porosity and surface roughness. *Fatigue Fract Eng Mater Struct*. 2019;42:2043–2052. <https://doi.org/10.1111/ffe.13077>